EurJIC
European Journal of Inorganic Chemistry

Full Paper
doi.org/10.1002/ejic.201901310

Single-Source Precursors

Ruthenium(II) MOCVD Precursors for Phosphorus-Doped Ruthenium Layer Formation

Andrea Preuß,[a] Jelena Tamuliene,[b] Katarzyna Madajska,[c] Iwona B. Szymanska,[c] Marcus Korb,[a][‡] Tobias Rüffer,[a] Janine Jeschke,[a] Marcel Melzer,[d,e] Jörn Bankwitz,[d,e] Stefan E. Schulz,[d,e] and Heinrich Lang*[a,f]

Abstract: The synthesis and solid-state structure of $Ru(CO)_2(PEt_3)_2(O_2CR)_2$ (**4a–f**, R = Me, Et, *i*Pr, ^{t}Bu, CH_2OMe, CF_3) is reported. The vapor pressure of **4a–f** was measured, ranging from 6.3 mbar (**4f**) to 14.8 at 190 °C (**4e**). Complexes **4a–f** decompose between 210–350 °C of which **4c** shows the lowest (248 °C) and **4e** (280 °C) the highest onset temperature. TG-MS studies (**4f**) showed subsequent decarbonylation and decarboxylation processes. To determine the gas phase composition VT IR studies were performed. Based on TG-MS, VT IR and DFT calculations decomposition mechanisms are discussed. Complexes **4a–f** are suited as MOCVD precursors, producing dense layers of 25–50 nm thickness, consisting of 57 at-% Ru, up to 18.2 at-% P and as impurities C, N and O. A carbon-free Ru(P) layer was obtained with **4a** as CVD precursor.

Introduction

In semiconductor industry the steady miniaturization of devices is a challenging task which depends on the need of new materials.[1] In this respect, ruthenium attracted recently attention as promising candidate for the replacement of currently used materials,[1] due to its high thermal and chemical robustness.[2] Furthermore, ruthenium is characterized by its low electrical resistance[2–4] and insignificant solid solubility with copper,[5–8] which makes ruthenium interesting as adhesion or seed layer for copper interconnects in the manufacturing of integrated circuits by the Damascene process.[7–11] Moreover, ruthenium has emerged as an alternative copper diffusion barrier.[5,6] However, thin films consisting of solely ruthenium are not applicable as copper diffusion barrier,[6,12–14] since Ru layers pursue the Volmer-Weber growth mechanism and show a polycrystalline columnar growth, due to their high surface energy.[8] Ruthenium films suffer from copper diffusion at unacceptable low temperature along the grain boundaries and hence layers consisting of nanocrystalline or amorphous textured ruthenium are needed.[5,8] One possibility for layer improvement is to dope ruthenium films with phosphorus, since such deposits provide a better inhibition of copper diffusion.[15–17] Density-functional theory (DFT) calculations reveal that an amorphous layer structure is favorable, when the film shows a content of 20 at-% phosphorus.[18–20]

Recently, a few studies for the formation of phosphorus-doped ruthenium layers by applying the PVD (= physical vapor deposition), CVD (= chemical vapor deposition) or ALD (= atomic layer deposition) process were reported.[16,17,21] In general, a dual source approach for Ru(P) thin film formation was implemented by using the triangular cluster $Ru_3(CO)_{12}$ and different phosphines as precursors.[17] The drawback of this method is, however, that the films contain up to 50 mol-% of carbon impurity,[22] which is influenced by the respective phosphine used as P source.[17,19] In addition, due to the different vapor pressure and reactivity of both precursors, a major variation in composition across the thickness of the layer is observed, especially in the respect of the phosphorus content.[19] To gain a better reproducibility of the layers, a single-source approach with a precursor containing both elements is favored because a better homogeneity and hence distribution of both elements within the layers is expected.[18,23,24] So far, only a few examples of single-source precursors exist, which are able to form Ru(P) layers.[18,23] However, layers deposited by the air-sensitive $RuH_2(PMe_3)_4$ coordination complex suffer from the incorporation of C, which lead to an increase of the film resistivity and therefore reduce the usability of the films as copper diffu-

[a] *Technische Universität Chemnitz, Faculty of Natural Sciences, Institute of Chemistry, Inorganic Chemistry, 09107 Chemnitz, Germany*
E-mail: heinrich.lang@chemie.tu-chemnitz.de
https://www.tu-chemnitz.de/chemie/anorg/
[b] *Vilnius University, Faculty of Physics, Institute of Theoretical Physics and Astronomy, 10222 Vilnius, Lithuania*
[c] *Faculty of Chemistry, Nicolaus Copernicus University, Gagarina 7, 87-100 Torun, Poland*
[d] *Fraunhofer Institute for Electronic Nano Systems (ENAS), Technologie-Campus 3, 09126 Chemnitz, Germany*
[e] *Technische Universität Chemnitz, Center for Microtechnologies, 09107 Chemnitz, Germany*
[f] *MAIN Research Center, Rosenbergstraße 6, 09126 Chemnitz, Germany*
[‡] Present address: The University of Western Australia, Faculty of Science, School of Molecular Sciences, Crawley, Perth, WA 6009, Australia
Supporting information and ORCID(s) from the author(s) for this article are available on the WWW under https://doi.org/10.1002/ejic.201901310.

sion barriers.[23] Nevertheless, the quality of the layers could be improved by using H_2 as reactive gas in the deposition process.[17]

Lately, our group reported about the synthesis as well as chemical and physical properties of ruthenium CVD precursors of type $Ru(CO)_2(P^nBu_3)_2(O_2CR)_2$ bearing different carboxylates as ligands, which allow to influence the thermal properties of the respective complexes.[15,25] In contrast to $RuH_2(PMe_3)_4$, the Ru precursors of type $Ru(CO)_2(P^nBu_3)_2(O_2CR)_2$ gave Ru(P) layers without the use of any reactive gas. As result thereof, 16 mol-% phosphorus-doped ruthenium layers could be obtained, but the deposits also suffer from carbon impurities of about 30 mol-%, whereby the branching and chain length of the respective carboxylates had only a minor influence.[15] This prompted us to synthesize a series of ruthenium precursors of type $Ru(CO)_2(PEt_3)_2(O_2CR)_2$, where P^nBu_3 is replaced by the PEt_3 ligand to decrease the carbon content of the precursors and therefore, to decrease the source of carbon impurities of the as-deposited layers.

We herein present the synthesis and characterization of ruthenium complexes $Ru(CO)_2(PEt_3)_2(O_2CR)_2$ (R = Me, Et, ^{i}Pr, ^{t}Bu, CH_2OMe, CF_3) and their use as a single-source CVD precursor for the formation of conformal and homogeneous phosphorus-doped Ru layers. Next to TG and TG-MS studies, in situ VT IR measurements were carried out to gain a deeper insight into the decomposition mechanism of the appropriate Ru^{II} complexes under reduced pressure. DFT calculations were additionally carried out to manifest the experimental results.

Results and Discussion

Synthesis and Characterization

Ruthenium complexes $Ru(CO)_2(PEt_3)_2(O_2CR)_2$ (**4a**, R = Me; **4b**, R = Et; **4c**, R = ^{i}Pr; **4d**, R = ^{t}Bu; **4e**, R = CH_2OMe; **4f**, R = CF_3) are accessible by the reaction of the triangular cluster $Ru_3(CO)_{12}$ (**1**) with PEt_3 (**2**) and subsequently addition of the respective carboxylic acid (**3a**–**f**) (Scheme 1).[26] After appropriate work-up, metal-organic compounds **4a**–**f** could be isolated as air and moisture stable colourless solids, which dissolve in most common organic solvents.

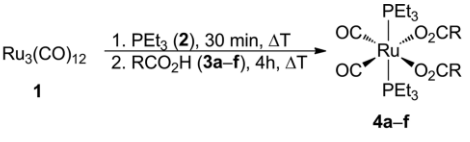

a: R = Me; **b**: R = Et; **c**: R = ^{i}Pr; **d**: R = ^{t}Bu; **e**: R = CH_2OMe; **f**: R = CF_3

Scheme 1. Synthesis of ruthenium complexes **4a**–**f** from **1**, **2**, and **3a**–**f**.

The identity of all complexes was confirmed by elemental analysis, IR, and NMR (^{1}H, ^{13}C{^{1}H}, ^{31}P{^{1}H}) spectroscopy and high resolution ESI-TOF mass spectrometry (Experimental Section). The molecular structures of **4a**–**f** in the solid-state were determined by single-crystal X-ray structure analysis. Further, the thermal behavior as well as the vapor pressure of the complexes were studied by thermogravimetric, thermogravimetric-coupled mass-spectrometric measurements and temperature variable infrared spectroscopy.

The ^{31}P{^{1}H} NMR spectra of **4a**–**f** exhibit one characteristic singlet for the PEt_3 groups ranging from 21.6 to 23.1 ppm (Experimental Section). The respective resonance signals are shifted to lower field as compared to free **2** (–20 ppm) and hence ^{31}P{^{1}H} NMR spectroscopy allows to monitor the progress of the reaction of **1** with **2** and **3a**–**f** to give **4a**–**f**.

The ^{1}H and ^{13}C{^{1}H} NMR spectra of **4a**–**f** are in accordance with the proposed structures (Experimental Section). Specific to the ^{13}C{^{1}H} NMR spectra is the splitting of the α-CH_2 groups of the PEt_3 ligands into triplets (J_{CP} = 13.5 Hz) (Experimental Section), which is a common phenomenon for the symmetry-related nuclei present in transition metal phosphine compounds.[15,27–29] This observation is based on the respective AA′XX′ spin system (A = P, X = C) occurring, when the coupling constant J_{PP} is significantly larger than that of J_{CP}, which was confirmed by calculations of Metzinger and Harris.[27,30,31]

In the IR spectra of ruthenium complexes **4a**–**f** two strong stretching vibrations for the terminal carbonyl groups are observed between 1970 and 2056 cm^{-1} (Experimental Section) confirming that the carbonyl groups are *cis*-oriented, since for *trans* isomers only the appearance of one stretching vibration is expected.[32] The binding mode of the carboxylate groups can be determined by the difference of the asymmetric (ν_{asym}) and symmetric (ν_{sym}) carboxylate CO_2 stretching vibrations.[33] The asymmetric frequencies are observed between 1600–1685 cm^{-1}, while the symmetric ones are observed at 1450–1465 cm^{-1} (Experimental Section). The asymmetric-symmetric band differences for all complexes is > 150 cm^{-1} indicating that the carboxylates are bonded to ruthenium in a monodentate fashion,[33] which was confirmed by single-crystal X-ray diffraction measurements (vide infra).

The molecular structures of **4a**–**f** in the solid-state were determined by single-crystal X-ray diffraction analysis. Suitable crystals were obtained from concentrated hexane/diethyl ether mixtures (ratio 10:1, *v*/*v*) at 10 °C. The ORTEPs of **4d** and **4f** are depicted in Figure 1, while the ones of **4a**–**c** and **4e** along with the key structural data can be found in the Supporting Information (SI; Figures S1–S4, Tables S1 and S2). The crystal and structure refinement data are presented in the Experimental Section.

The respective complexes crystallize in monoclinic space groups $P2_1/n$ (**4a**) and $P2_1/c$ (**4c**, **4f**), in the triclinic space group $P\bar{1}$ (**4b**, **4d**) as well as in the orthorhombic space group $Pca2_1$ (**4e**), with one crystallographically independent molecule in the asymmetric unit.

The complexes consist of a slightly distorted octahedral coordinated ruthenium atom with two *trans*-positioned triethylphosphines (P1 and P2) in the apical positions, two *cis*-oriented carbonyls and two *cis*-monodentate O-bonded carboxylates in the equatorial plane (Figure 1 and Figures S1–S4). The phosphines slightly bent towards the carboxylates with angles of 174.60(5) to 176.22(4)°, which is in good agreement with recently reported ruthenium complexes of this type.[15,27,28] The carbonyl entities of the respective carboxylates are rotated away from each other to avoid electronic interactions. Therefore, this arrangement effects the angles in the equatorial plane,

Full Paper
doi.org/10.1002/ejic.201901310

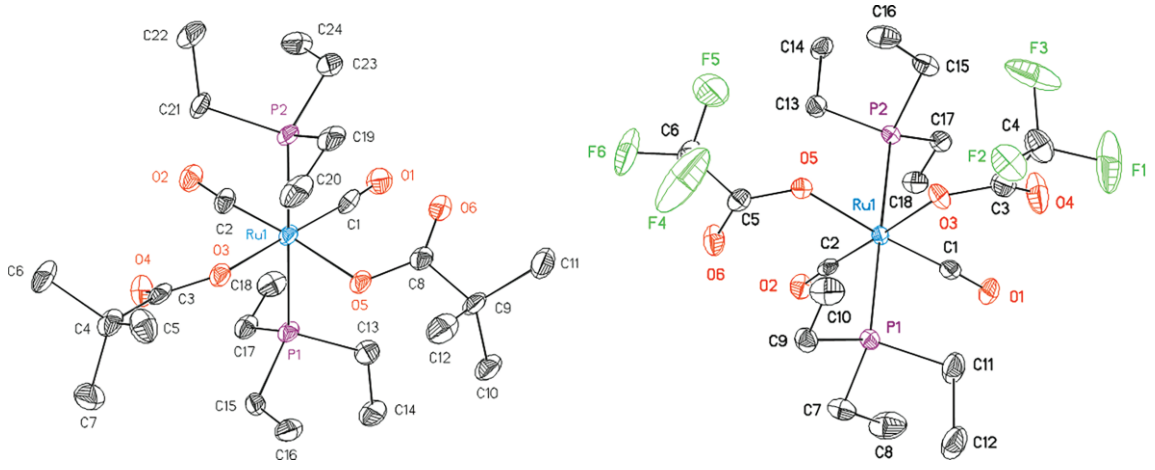

Figure 1. ORTEPs (50 % probability level) of the molecular structure of **4d** (left) and **4f** (right) with the atom numbering scheme. All hydrogen and disordered atoms have been omitted for clarity.

whereby the O–Ru–O and C–Ru–C angles are decreased to 80.11(13)–84.20(12)° (O–Ru–O) and 87.88(5)–89.6(4)° (C–Ru–C), whereas the C–Ru–O angle is increased to values ranging from 92.97(13) to 96.32(19)°. The classification in single and double bonds within the carboxylate ligand is possible by comparing the distances of the C–O bond lengths. For the C–O bond, where the oxygen binds to the ruthenium atom, values were observed between 1.267(5) to 1.300(11) Å indicating a single bond. In contrast to that, C–O distances of 1.213(5) to 1.232(2) Å were determined for the carbonyl unit of the carboxylate ligand confirming a double bond. This binding motif was also verified by IR spectroscopy (see above).

In **4a**–**f** the carboxylate CO units are directed *anti* with regard to the equatorial plane. Similar observations were made for analogous triphenylphosphine and tri-*n*-butylphosphine ruthenium complexes.[15,27,28]

The rms deviations of the calculated RuC_2O_2 planes range from 0.0182 (**4b**) to 0.043 (**4c**) (Table S3), which are rather high values reflecting a distortion of the equatorial plane with the ligands slightly bending out of it.

Thermal Decomposition

Thermogravimetric Studies of 4a–f

To gain first information on the thermal behavior of complexes **4a**–**f** thermogravimetric (TG) studies were carried out. The physical properties of **4a**–**f** are summarized in Table 2. The TG measurements were carried out in an atmosphere of nitrogen (gas flow of 20 mL min^{-1}) with an additional continuous nitrogen carrier gas flow of 40 mL min^{-1} in the temperature range of 40–600 °C.

From the respective traces (Figure 2) it can be seen that all complexes show a weight loss between 210 and 350 °C, due to their decomposition. Within this series it can be seen that the chain length or branching of the carboxylate ligands has no significant influence on the decomposition process, resulting in comparable onset temperatures of approximately 250 °C (Figure 2 and Table 2). Contrary, complex **4e** featuring the CH_2OMe substituent shows the highest onset temperature of all compounds (Figure 2, Table 2).

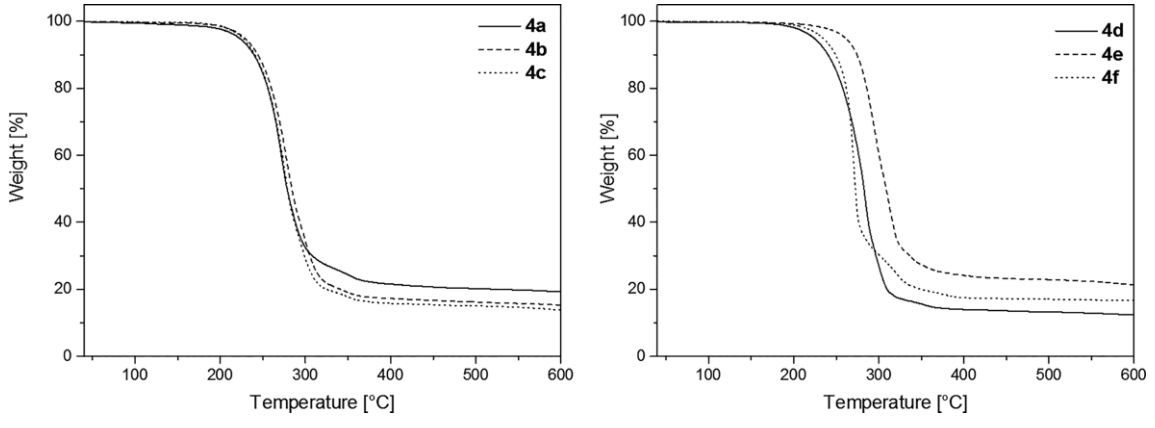

Figure 2. TG traces of **4a**–**c** (left) and **4d**–**f** (right); gas flow, N_2 20 mL min^{-1}, heating rate 10 °C min^{-1}.

Thermogravimetry-Mass-Spectrometry Studies of 4f

TG-MS (= thermogravimetry–mass-spectrometry) experiments were carried out on the example of **4f** for a better understanding of the decomposition behavior of **4a**–**f**. In Figure 3 the TG-MS traces containing the TG trace, the first derivative of the TG trace as well as the ion current curves of the appropriate mass-to-charge ratios (*m/z*) are shown. The detected ions with the related *m/z* values are given in the caption of Figure 3. From this Figure it can be seen that **4f** decomposes between 200 and 450 °C in multi-steps in contrast to the TG studies carried out with a heating rate of 10 °C min^{-1} (Figure 2). Lowering the heating rate from 10 (Figure 2) over 5 (Figure 3) to 2.5 °C min^{-1} (Figure S5, see the SI) led to a decrease of the onset temperature from 260 over 250 to 235 °C. The first weight loss of 15.3 % occurs at ca. 190 °C with the observation of fragments *m/z* = 15 (CH_3^+), 29 ($C_2H_5^+$) and 43 (CH_3CO^+) (Figure 3), emphasizing the cleavage of Ru–C, P–C and C–C bonds. The detection of CH_3CO^+ is due to recombination of CH_3 and CO radicals. At temperatures above 200 °C also the fragment *m/z* = 44 was formed corresponding to CO_2^+, confirming decarboxylation. Moreover, at this temperature also fragments with *m/z* = 50 (CF_2^+), 51 (CHF_2^+) and 69 (CF_3^+) were found (Figure 3) supporting the ongoing decomposition of **4f**. The highest weight loss of 52.2 % is observed at an onset temperature of 250 °C indicating the steady degradation of **4f** which is strengthened by the observation of fragments with *m/z* = 12 (C^+), 15 (CH_3^+), 26 ($C_2H_2^+$), 29 ($C_2H_5^+$), 30 ($C_2H_6^+$), 43 (CH_3CO^+), 44 (CO_2^+), 50 (CF_2^+), 51 (CHF_2^+) and 69 (CF_3^+). The decomposition of **4f** is completed at 500 °C as the intensities of every fragment decrease significantly at this point.

Theoretical Studies of 4a–f

In addition to TG and TG-MS measurements, density functional theory (DFT) calculations were carried out to encourage and clarify the mechanistic insights of the thermal decomposition studies (see earlier).

It was found that the different substituents R at the carboxylic groups do not significantly affect the thermal stability of the respective ruthenium complexes, i.e. their binding energy per atoms (BDE) is varied from 4.730 eV (**4e**) to 4.772 eV (**4d**) (Table 1).

The BDE values allow to predict the decomposition of **4f** as the most energy consuming one (Table 1). Hence, **4f** was chosen to study the decomposition process in detail to retrace the results from TG-MS studies (vide supra).

The results of the simulation for **4a**–**f** indicate that the first CO is released at the beginning of the heating process of the complex, whereby the energy of appearance of CO varies from 0.978 eV (**4c**) to 1.216 eV (**4f**). The release of one CO ligand leads to the rearrangement of the carboxylate and, as consequence thereof, to the decomposition of **4f**. Within this rearrangement process one of the two carboxylates changes from the monodentate to a chelating mode. The analysis of the energy of appearance of various fragments such as CO, CO_2CF_3, PEt_3 and the follow-up decomposition of the carboxylate fragment to give CO_2, CF_3 etc. indicates the spontaneous decarboxylation of the carboxylates forming CO_2 and R as the most energetically favorable process.

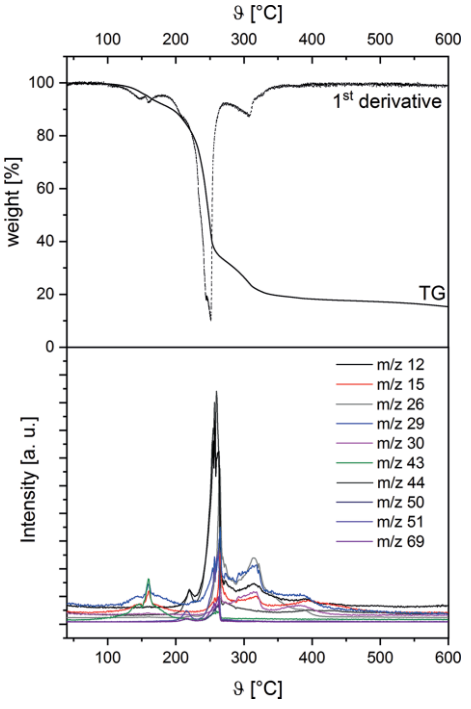

Figure 3. TG-MS traces of **4f** under an atmosphere of argon, gas flow, Ar 20 mL min^{-1}, heating rate 5 °C min^{-1}, ion current of *m/z* 12 (C^+), 15 (CH_3^+), 26 ($C_2H_2^+$), 29 ($C_2H_5^+$), 30 ($C_2H_6^+$), 43 (CH_3CO^+), 44 (CO_2^+), 50 (CF_2^+), 51 (CHF_2^+) and 69 (CF_3^+).

Table 1. The binding energy per atoms (BDE) of **4a**–**f** and that of the respective carboxylic acids.

Comp.	BDE [eV]	Carboxylic acids	BDE [eV]
4a	4.760	HO_2CMe	4.660
4b	4.765	HO_2CEt	4.787
4c	4.769	HO_2CiPr	4.802
4d	4.772	HO_2CtBu	4.811
4e	4.730	HO_2CCH_2OMe	4.692
4f	4.770	HO_2CCF_3	4.985

The energy of appearance of the remaining carboxylate at Ru is equal to 0.672 eV and is smaller than that of other fragments like CO, CF_3, O_2CCF_3 and combinations thereof. This emphasizes that the release of CO initiates the decarboxylation of the carboxylate ligands and hence the formation of carbon dioxide.

Two competitive decomposition processes of the as-formed intermediate $Ru(CO)(PEt_3)_2(CF_3)_2$ are observed based on theoretical studies. The energies of the appearance of CO and that of PEt_3 are equal to 1.314 eV and 1.332 eV, respectively. The difference of these energies is equal to 0.018 eV which is very close to the value of the thermal motion with $kT \approx 0.025$ eV and shows that the PEt_3 release from $Ru(CO)(PEt_3)_2(CF_3)_2$ is more likely at higher temperature. If CO is released from $Ru(CO)(PEt_3)_2(CF_3)_2$ the order of fragment formation are as follows: 1st PEt_3 (energy of appearance = 1.142 eV), 2nd PEt_3 (2.752 eV) and 3rd 2 CF_3 groups (spontaneous process). If PEt_3 is eliminated first than CO is split off (energy of appearance = 1.189 eV) followed by the second PEt_3 group being eliminated (2.752 eV) and afterwards the two CF_3 units (spontaneous proc-

ess). The total energy of the appearance of Ru from **4f** is varied from 7.096 eV to 7.61 eV and it is larger than that for **4b** and **4c**. For example, the calculated energy of appearance of Ru is equal to 5.601 eV as calculated for **4c** eliminating one CO ligand. The theoretical study of **4c** also indicates the possibility of formation of differently charged (neutral and positive) PEt_3 species which could be the reason for the presence of P^{III} and P^{V} in the phosphorus-doped ruthenium layers.

VT IR Studies of 4c,e,f

VT (variable temperature) IR studies have been carried out to study the composition of the gas phase when heating **4c**, **4e**, and **4f** over the temperature range of 30–380 °C under dynamic vacuum (p = 1 mbar).

Analysis of the IR spectra showed two CO bands at 2038 and 1974 cm^{-1} and an asymmetric COO stretching vibration at 1610 cm^{-1} between 180 and 260 °C for **4c**. Therefore, the presence of **4c** in the gase phase is confirmed.

However, in the temperature range of 180–220 °C bands typical for decomposition products such as CO (2170, 2116 cm^{-1}), $O{=}PEt_3$ (1131 cm^{-1}, $\nu_{(POC)}$; 667 cm^{-1}, $\nu_{s(PC)}$) and aldehyde (1752 cm^{-1}, $\nu_{(C=O)}$) are observed (stage I), of which the occurrence of aldehyde and phosphine oxide results from the reaction between PEt_3 and the respective carboxylate.

Moreover, the release of CO from **4c** led to the formation of the mononuclear ruthenium complex $[Ru(CO)(PEt_3)_2(\mu\text{-}O_2C^iPr)(O_2C^iPr)]$ (Scheme 2), whereby the free coordination unit is saturated by the chelation of one carboxylate as also proposed by DFT calculations (vide supra).

Upon further heating (240–300 °C), in addition to the aforementioned species, CO_2 (2335 cm^{-1}) could be detected in the gas phase (Figure 4, stage II) confirming initiation of decarboxylation of the respective species. A further set of CO frequencies at 2011, 1962 and 1939 cm^{-1} and an asymmetric COO stretching vibration at 1572 cm^{-1} were observed pointing to a bridging mode of the carboxylate (Figure 4, stage II). On this account

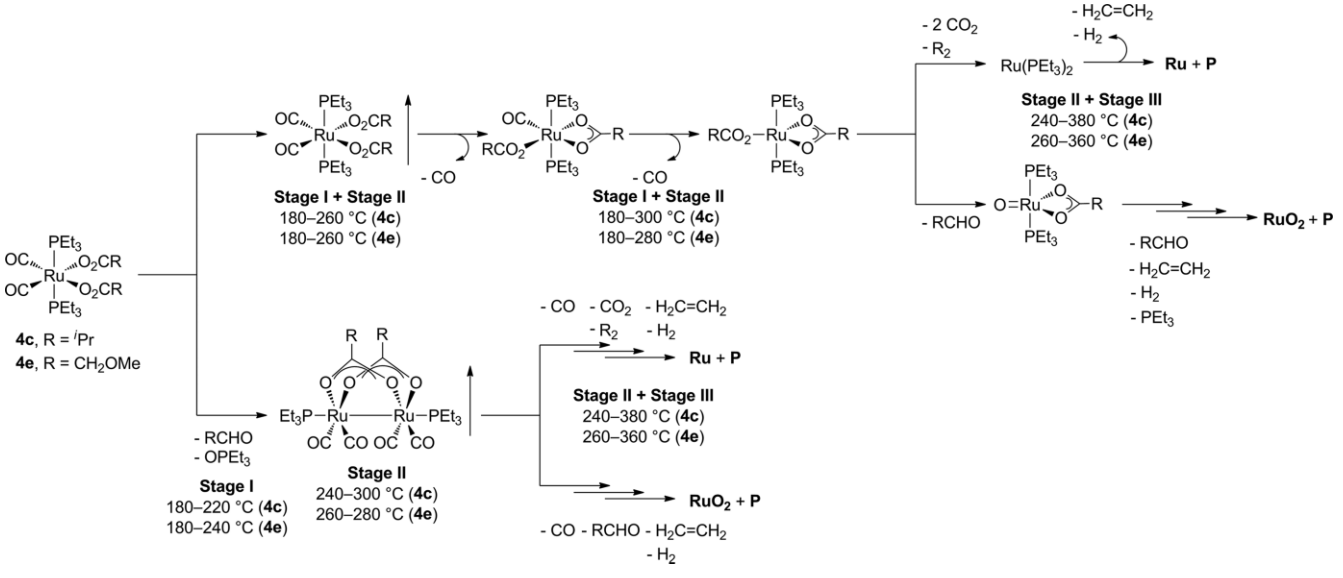

Scheme 2. Proposed decomposition mechanisms for **4c** and **4e**.

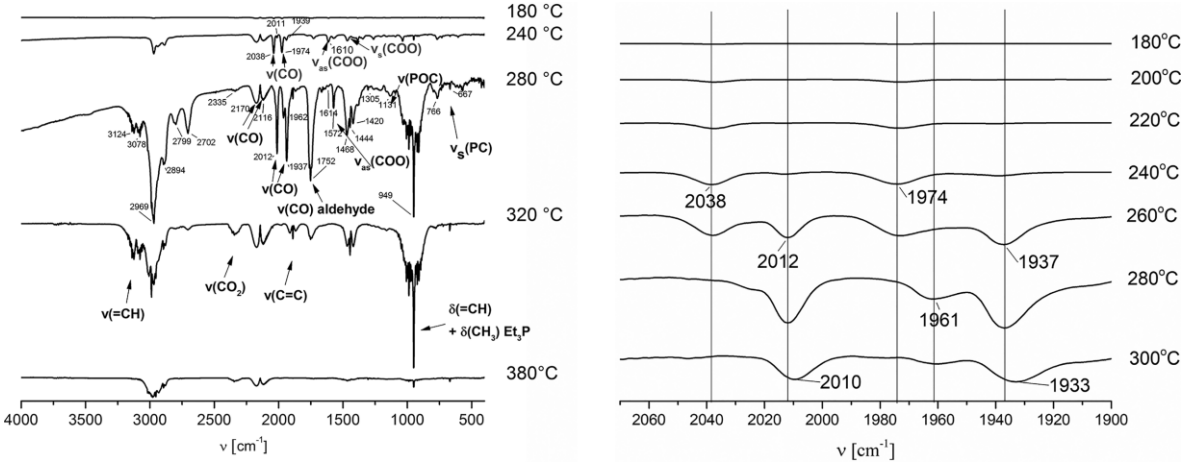

Figure 4. VT IR spectra of vapors formed during the heating of **4c** (temperature range 30–380 °C, p = 1 mbar). The characteristic bands of **4c** are marked in green.

the formation of homodinuclear ruthenium complexes, i.e. $[Ru_2(PEt_3)_2(CO)_4(\mu\text{-}O_2CiPr)_2]$ in the gas phase is suggested (Scheme 2).[35] This indicates that between 240 and 260 °C, two ruthenium complexes (mono- and dinuclear, Scheme 2) are present in the gas phase.

Between 320 and 380 °C distinctive vibrations (3124 cm^{-1}, $\nu_{(=CH)}$; 949 cm^{-1}, $\delta_{(=CH)}$) have been found confirming the formation of ethylene, which was formed via β-hydride elimination from the C_2H_5 groups during the thermal decomposition of PEt_3.[36]

Therefore, as appropriate residues Ru, RuO_2 and P are suggested (Scheme 2), which is in accordance with the results from CVD experiments (vide infra).

A similar decomposition process was found for **4e** in the temperature ranges 180–240 °C (Figure 5, stage I), 260–280 °C (Figure 5, stage II) and 300–360 °C (Figure 5, stage III), respectively (Figure 5, Scheme 2).

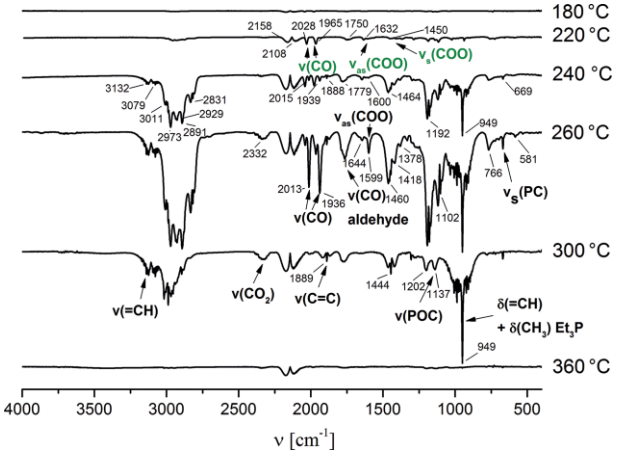

Figure 5. VT IR spectra of vapors formed during the heating of **4e** (temperature range 30–380 °C, p = 1 mbar). The characteristic bands of **4e** are marked in green.

The VT IR studies of **4f** indicated that this complex can be evaporated without decomposition by heating it over the temperature range of 160–200 °C (Figure 6). Degradation of **4f** starts at 220 °C (Figure 6) at which CO (2172 and 2117 cm^{-1}) and PEt_3 (951 and 666 cm^{-1}) are released, which is in accordance to TG-MS studies (vide supra).

Upon further heating two additional CO bands at 2029 and 1954 cm^{-1} and $\nu_{as(COO)}$ at 1599 cm^{-1} are observed, indicating the in situ chelation of the O_2CCF_3 entity forming complexes $Ru(CO)_2(PEt_3)(\mu\text{-}O_2CCF_3)(O_2CCF_3)$ and $Ru(CO)(PEt_3)_2(\mu\text{-}O_2CCF_3)(O_2CCF_3)$, respectively. At a temperature of 240 °C, molecules CO (2172 cm^{-1}, 2116 cm^{-1}), CO_2 (2346 cm^{-1}), CF_3CO_2H ($\nu_{as(COO)}$ = 1830 cm^{-1}) and $(F_3CCO)_2O$ ($\nu_{(CO)}$ = 1899 cm^{-1}) could be detected (Figure 6). Increasing the temperature to 340 °C resulted in the release of CO, PEt_3, $H_2C{=}CH_2$ (3125 cm^{-1}, $\nu_{(=CH)}$; 949 cm^{-1}, $\delta_{(=CH)}$), CF_3H (1153 cm^{-1}) and aliphatic mono-fluorinated compounds (1028 cm^{-1}). The formation of ethylene and trifluoromethane results from the reaction of the C_2H_5 group from the PEt_3 and the CF_3 group from the carboxylate. Between 360–380 °C (Figure 6) aliphatic mono-fluorinated species are the main components found in the gas phase. The as-formed solid composes of Ru, RuO_2 and P.

The analysis of the VT IR spectra demonstrated the presence of complexes **4c**,**e**,**f** in the gas phase over the temperature range of 180–260 °C (**4c**, **4e**) and 120–240 °C (**4f**). However, **4c** and **4e** begin to decompose during evaporation contrary to **4f**, which indicates a lower thermal stability of **4c** and **4e** under the applied measurement conditions. In addition, other gaseous species were observed for **4c** and **4e** than for **4f**, which reflects an influence of fluorination of the carboxylate on the thermal behavior. The final solid degradation products for all studied complexes are Ru, RuO_2 and P.

Vapor Pressure Measurements

Vapor pressure measurements were carried out on compounds **4a**–**f** to demonstrate if the complexes are suited to be used as CVD precursors. The method applied is based on the mass loss of the samples as a function of increasing temperature at atmospheric pressure (Experimental Section).[2] Hence, a TG system with a horizontal balance was used to determine the

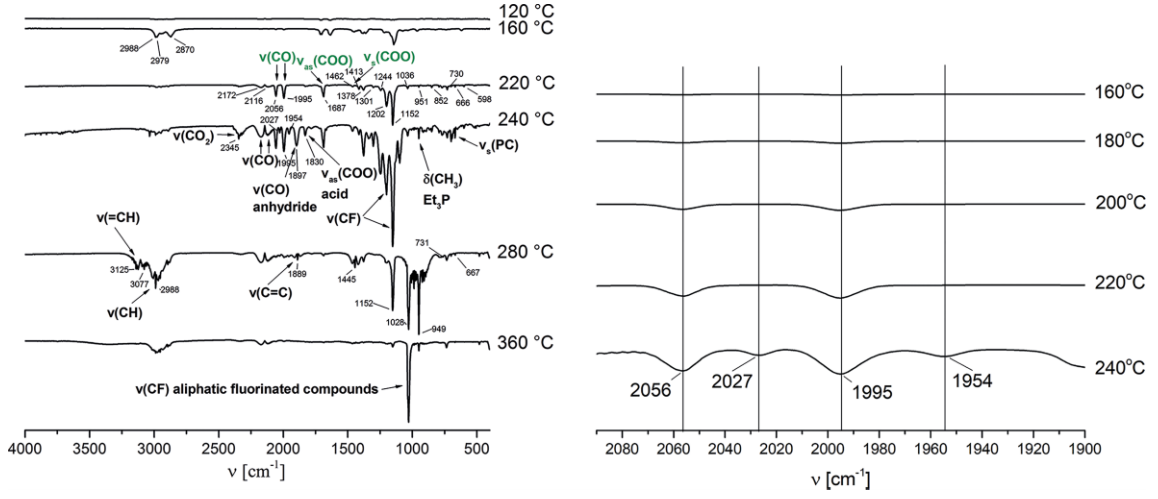

Figure 6. VT IR spectra of vapors formed during heating of **4f** (temperature range 30–380 °C, p = 1 mbar). The characteristic bands of **4f** are marked in green.

Full Paper
doi.org/10.1002/ejic.201901310

weight loss in an isothermal phase at different temperatures as reported in reference [2]. To diminish the measurement errors and provide reliable experimental data, each study was carried out thrice.

All complexes show volatility within the applied temperature range (**4a**–**4e**, 160–260 °C; **4f**, 180–220 °C), which was chosen according to the TG studies (Figure 2) to avoid decomposition during the vapor pressure studies. The respective results are depicted in Figure 7. Furthermore, the measurements allowed the determination of the Antoine parameters, which are summarized in Table 2.

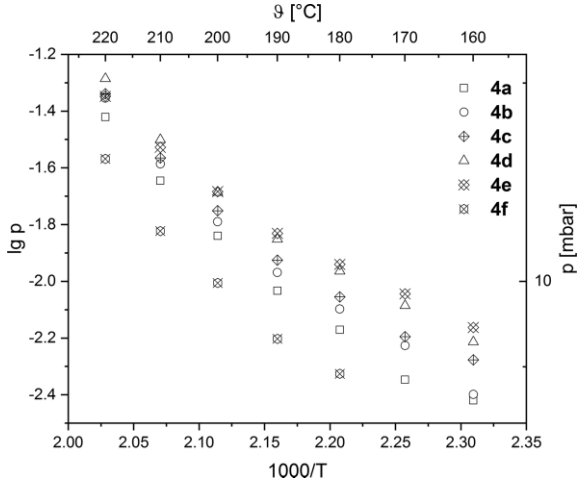

Figure 7. Vapor pressure traces of **4a**–**f** in an atmosphere of nitrogen (40 mL min^{-1}).

Table 2. Physical properties of compounds **4a**–**f**.

Compd.	M.p. [°C]	Onset [°C]	log *p* [bar] = *A* − *B*/*T*[a] *A*	*B*	R^2	ΔH_{vap} [kJ mol^{-1}]	$p_{190\ °C}$ [mbar]
4a	124.5	255	5.78	3589	0.9699	68.7	9.3
4b	133.5	249	5.84	3585	0.9764	68.6	10.7
4c	142.0	248	5.31	3319	0.9634	63.5	11.9
4d	135.0	258	5.14	3209	0.9698	61.4	14.1
4e	111.5	280	4.34	2835	0.9767	54.3	14.8
4f	165.0	260	6.94	4218	0.9741	80.8	6.3

[a] *A* and *B* = Antoine parameters; *T* = absolute temperature; R^2 = coefficient of determination.

The highest volatility at 190 °C was observed for **4d** (R = ^{t}Bu) and **4e** (R = CH_2OMe) (Table 2), while **4f** shows the lowest volatility of all ruthenium species. It is known that the low polarizability of the C–F bonds leads to reduced intermolecular interactions within the compounds.[34] In the series of **4a**–**d** the influence of the respective carboxylate ligands is observable, whereby the increase of the chain length and the branching results in higher vapor pressures. The herein presented ruthenium complexes exhibit a similar volatility compared to previously reported ruthenocenes or half-open ruthenocenes[2] as well as $Ru(CO)_2(P^nBu_3)_2(O_2CR)_2$[15] (e.g., R = Me, Et, ^{i}Pr).

Chemical Vapor Deposition

The deposition of phosphorus-doped ruthenium layers was successfully carried out with compounds **4a**–**f** as CVD precursors. For these studies a home-built vertical cold-wall reactor equipped with a continuous evaporation system was applied.[2] The depositions were performed using nitrogen as carrier gas (60 mL min^{-1}; 0.9 mbar working pressure). For the deposition experiments Si wafers covered with a continous 100 nm thick thermal SiO_2 layer were used. The evaporation temperature of the precursor complexes was set to 125–165 °C in the vaporizer unit. The glass lines were heated to 100 °C. The substrate temperature was selected according to the results of the TG studies (vide supra) and hence was set to 350 °C. The MOCVD deposition parameters of the obtained layers **A**–**F** are summarized in Table 3. Depending on the used precursors, film thicknesses of 25 nm (**4a**,**c** and **4d**) up to 50 nm (**4b**,**e** and **f**) were obtained. The 25 nm thin films are reflective and metallic and thicker films are yellowish.

Table 3. Deposition parameters of layers **A**–**F** deposited from **4a**–**f**.[a]

Layer	Compd.	$\vartheta_{(Prec.)}$ [°C]	N_2 flow [mL min^{-1}]	Layer thickness[b] [nm]
A	**4a**	125	50	25
B	**4b**	135	60	50
C	**4c**	145	60	25
D	**4d**	128	60	25
E	**4e**	145	60	49
F	**4f**	165	60	50

[a] Substrate temperature was set to 350 °C and the deposition was carried out for 45 min at pressures between 0.9–1.0 mbar. [b] Determined by cross-sectional SEM images.

Layer Characterization

The morphology and chemical composition of the as-deposited layers were studied by using SEM (scanning electron microscopy) (Figure 8 and Figures S6–S11, see the SI), EDX (energy-dispersive X-ray spectroscopy) (Figures S12–S17) and XPS (X-ray photoelectron spectroscopy) (Figure 9 and Figures S18–S23, see the SI).

SEM studies show the formation of dense and conformal layers for all investigated films deposited from **4a**–**f** (Figure 8), whereby the topography of the produced layers **A**–**F** is quite similar showing no optical differences in the homogeneity or roughness. The film thicknesses were determined by cross-sectional SEM images (Table 3 and Figures S6–S11, see the SI). The highest growth rates were observed for **4b**,**e** and **4f**. The appearance of the as-deposited layers **A**–**F** are comparable to the one obtained by using $Ru(CO)_2(P^nBu_3)_2(O_2CR)_2$ as CVD precursor.[15]

The chemical composition of layers **A**–**F** was analyzed by EDX spectroscopy using different electron beam energies (3 and 6 keV) (Figures S12–S17, see the SI). For all layers the characteristic pattern of ruthenium was observed (Figures S12–S17). In addition, the presence of phosphorus, silicon, oxygen and carbon was detected and in the case of layer **E** also nitrogen could be found (Figure S16). It should be noted that silicon and part of the oxygen originate from the Si/SiO_2 substrates, which is strengthened by the decrease of the signal intensity, when using decreased electron beam energy.

Full Paper
doi.org/10.1002/ejic.201901310

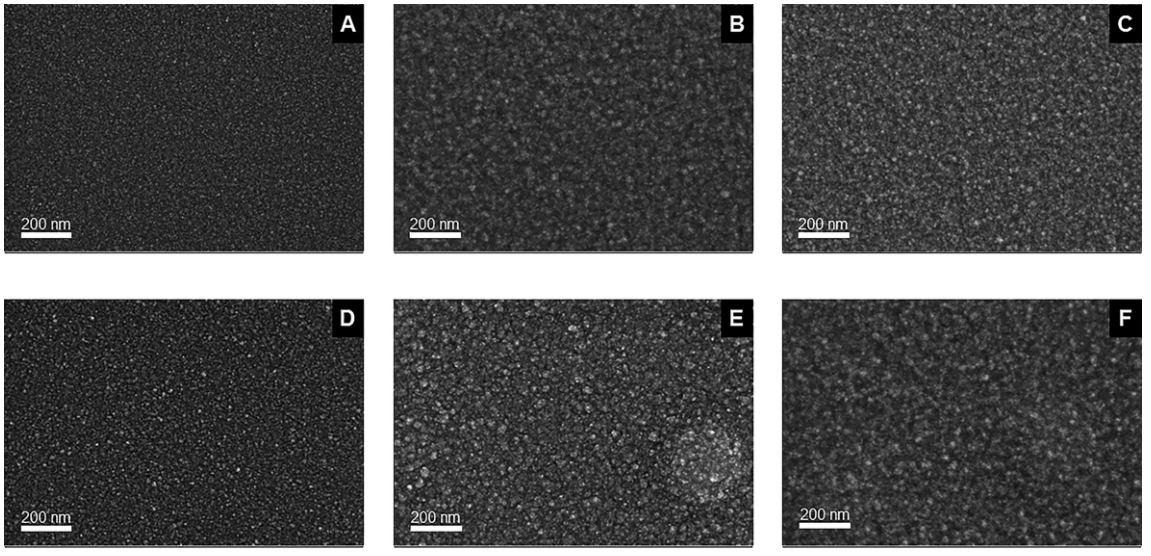

Figure 8. SEM images (magnification: 80 000 ×) of ruthenium films **A**–**F** deposited on SiO_2 using the parameters given in Table 3. **A**: **4a**, **B**: **4b**, **C**: **4c**, **D**: **4d**, **E**: **4e**, **F**: **4f**.

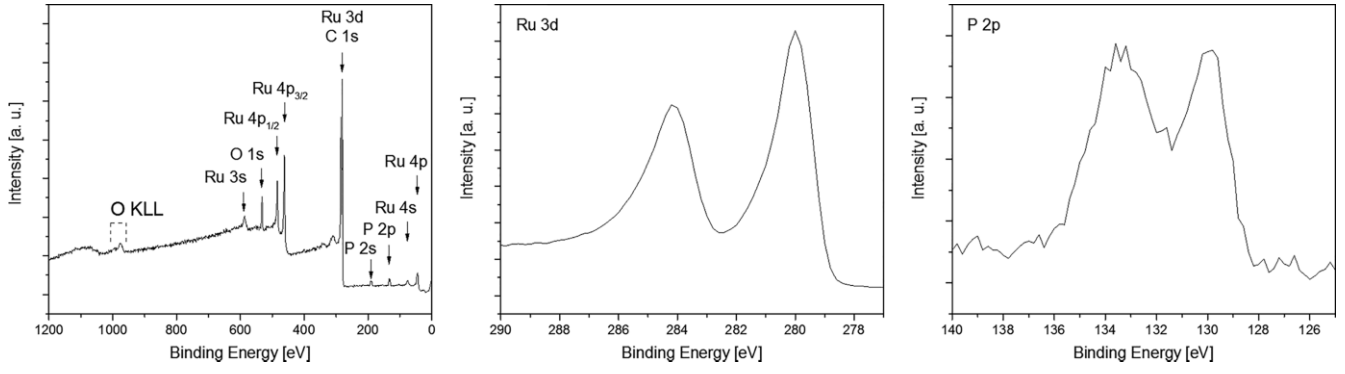

Figure 9. XPS survey spectrum of layer **B** (left); detailed XPS spectra of the Ru 3d (middle) and P 2p peaks (right) of layer **B** obtained by using **4b** as CVD precursor.

The determination of the film composition without penetration of the Si/SiO_2 wafer was carried out applying surface sensitive *ex situ* XPS measurements. The results are summarized in Table 4 and exemplary a typical XPS spectrum and detailed XPS spectra of the Ru 3d and P 2p peaks of layer **B** obtained from **4b** are depicted in Figure 9. The XPS spectra of all other samples are presented in the SI (Figures S18–S23).

Table 4. Elemental composition of layers **A**–**F**.

	Layer composition[a] [at.%]				
Layer	Ru 3d	P 2p	C 1s	O 1s	N 1s
A	56.6	17.0	0.0	26.3	0.0
B	45.4	18.2	5.4	26.5	4.5
C	44.2	15.4	6.0	29.7	4.7
D	47.4	21.8	7.3	23.4	0.0
E	30.7	16.2	30.5	22.6	0.0
F	21.5	16.3	28.6	33.7	0.0

As it can be seen from Table 4, no silicon was detected for all investigated deposits (for comparison see the EDX studies, vide supra), instead Ru, P, O and C were found. Furthermore, it should be noted that layer **F** is fluorine-free as no fluorine could be detected either by EDX nor XPS analysis, which is beneficial with regard to the prospective use as copper diffusion barrier, since once fluorine is incorporated in the layer it can damage the electronic properties of the devices.[37]

Sputtering (4.0 keV, 330 s) was performed to remove surface contaminations. The Ru 3d peak splits into two peaks at 284.2 eV (Ru $3d_{3/2}$) and 280 eV (Ru $3d_{5/2}$), due to spin-orbital interactions (Figure 9). These values are in agreement with the ones listed in the XPS binding energy database and correspond to metallic ruthenium.[38,39] The Ru 3d peaks overlap with the C 1s peak at 284.5 eV.[40] For the determination of the carbon content a peak deconvolution was carried out for the Ru 3d doublet and the C 1s peak. The used parameters with respect to the peak shape and peak position, which were applied for the deconvolution, are summarized in Table S4 (see the SI). For all peaks a maximum FWHM of 2.0 eV was allowed. Furthermore, the area ratio of both metallic and non-metallic Ru $3d_{3/2}$ and Ru $3d_{5/2}$ peaks was fixed to 2:3 and the peak separation between $3d_{5/2}$ and $3d_{3/2}$ to 4.2 eV.[41] For the identification of peak splitting with respect to P 2p and O 1s a Gaussian–

Lorentzian peak shape was applied with a Lorentzian contribution of 25 %.

The as-obtained layers consist of 22–58 at-% Ru, 15–22 at-% P, 23–34 at-% O and 0–31 at-% C (Table 4). Besides Ru, ruthenium oxide is present, which is confirmed by the $3d_{5/2}$ peak at 281.0 eV.[40] Considering that the deposition experiments were performed in an inert gas atmosphere, the presence of RuO_2 in the layers most likely originates from remaining oxygen from the dissociation of the carboxylate or the CO ligands.[15,42,43] The detailed XPS spectra of the P 2p peak confirms the presence of P^{III} (130.2 eV)[38] and P^{V} (133.3 eV)[44,45] (phosphine oxide species) (Figure 6). Due to the small energy difference of 0.3 eV between P^{III} and P^{0} (129.9 eV)[38] it can not be excluded that elemental phosphorus is present in the layers, too. In case of phosphorus-doped ruthenium layers reported by Jeschke et al. only at the surface of the layers P^{V} was observed, due to oxidation processes of the topmost layer.[15] Within the layers the XPS analyses reveal only elemental phosphorus.[15] The carbon content of layers **A**–**F** increases from 0 at-% (layer **A**) up to 30.5 at-% (layer **E**). The incorporated carbon is a result of the catalytic properties of the ruthenium surface leading to C–C and C–H activation of absorbed ligands.[46,47] Within the series of **4a**–**d** the increase of the carbon content can further be assigned to the increase of carbon within the precursors itself.

In layers **B** and **C** approximately 5 at-% of nitrogen could be detected, which arises from the adsorption of the carrier gas applied during the CVD process. Jacobi et al. reported within the ammonia synthesis using ruthenium as catalyst, the rate-determining step is the dissociative adsorption of N_2.[48] Therefore, the adsorption of N_2 during deposition without desorption, due to faster layer growth, might be the reason for nitrogen incorporations of layers **B** and **C**.

Conclusion

The formation of phosphorus-doped ruthenium layers via CVD was successfully achieved by using the single-source precursors $Ru(CO)_2(PEt_3)_2(O_2CR)_2$ (**4a**, R = Me; **4b**, R = Et; **4c**, R = *i*Pr; **4d**, R = *t*Bu; **4e**, R = CH_2OMe; **4f**, R = CF_3), which could be obtained by a "one-pot" reaction of $Ru_3(CO)_{12}$, PEt_3 and the respective carboxylic acids.

TG studies revealed that the decomposition of **4a**–**f** occurs between 210–350 °C, whereof **4e** shows an increased onset temperature at 280 °C. Vapor pressure measurements demonstrated that all complexes are volatile between 180–220 °C. The vapor pressures within the series of **4a**–**d** are influenced by the branching and chain length of the respective carboxylate ligands resulting in the highest vapor pressure for **4d** of 14.1 mbar at 190 °C. Unexpectedly, **4f** featuring CF_3 substituents shows the lowest vapor pressure of all investigated compounds.

The thermal decomposition of the ruthenium complexes was studied by TG-MS, VT IR spectroscopy and DFT calculations. TG-MS and DFT investigations emphasized that during thermal decomposition of **4f** first a decarbonylation occurs with subsequent decarboxylation. Analysis of the VT IR spectra demonstrated that all studied compounds are volatile but for the non-fluorinated ones (**4c**, **e**) parallely decomposition occurs. Moreover, different gaseous products were detected for the non-fluorinated and fluorinated complexes. Therefore, for **4c**,**e** and **4f** two different degradation mechanisms are proposed but the final decomposition products consisted of Ru, RuO_2 and P.

Deposition experiments were carried out in a cold-wall CVD reactor at deposition temperatures of 350 °C in an inert gas atmosphere without the need of any additional phosphorus source or reactive gas. The highest growth rates were observed for **4b**,**e**,**f**. All received films were dense and conformal as proven by SEM studies and the elemental composition was analyzed by EDX and XPS. Thereby, it should be noted that layer **A** deposited from **4a** is carbon-free. For the formation of phosphorus-doped ruthenium layers the single-source ruthenium complexes **4a**–**f** show promising properties, as the compounds are easy accessible and do not need any reactive gas during the deposition process. Furthermore, the PEt_3 ligands led to the formation of layers with phosphorus contents of up to 18.2 at-%, which make them attractive as copper diffusion barrier in the fabrication of integrated circuit.

Experimental Section

Instruments and Materials

All synthesis procedures were performed under an atmosphere of argon with the solvents degassed prior to use. All reagents were obtained from commercial suppliers and used without further purification.

NMR spectra were recorded using a Bruker Avance III 500 spectrometer operating an 500.3 MHz for ^1H, 125.7 MHz for $^{13}C\{^1H\}$ and 202.5 MHz for $^{31}P\{^1H\}$ in the Fourier transform mode at 293 K. Chemical shifts are reported in δ (ppm) downfield from tetramethysilane with the solvent as reference signal (^1H NMR, $CDCl_3$ δ = 7.26 ppm; $^{13}C\{^1H\}$ NMR δ = 77.16 ppm; $^{31}P\{^1H\}$ NMR, standard external relative to 85 % H_3PO_4 δ = 0.00 ppm $^{31}P\{^1H\}$). FT-IR spectra were recorded with a Thermo Nicolet IR 200 instrument. The melting points were determined using a Gallenkamp MFB 595 010 M melting point apparatus. Elemental analyses were performed by using a thermos FlashAE 1112 instrument. High-resolution mass spectra were recorded with a Bruker Daltonite micrOTOF-QII spectrometer by electro-spray ionization.

TG experiments and vapor pressure studies were performed using a Mettler Toledo TGA/DSC1 1100 system with a UMX1 balance. The TG-MS investigations were performed with a Mettler Toledo TGA/DSC1 1600 equipment with a MX1 balance coupled with a Pfeifer Vacuum MS Thermostar GSD 301 T2 mass spectrometer. CVD experiments were carried out with a home-built vertical cold-wall CVD reactor with heater dimension of 20 × 20 mm (BACH Resistor Ceramics GmbH). Heating was adjusted up to 500 °C and was controlled by a Gefran 600 module connected with a Pt100 thermosensor. The carrier gas (N_2) was controlled by MKS type 247 mass flow controllers connected to the reactor by heated copper lines. The CVD system was attached to a rotary vane pump RZ 6 (Vacuubrand). The pressure of the reactor system was controlled by the Vacuubrand vacuum controller CVC 3000 in combination with an external Pirani vacuum sensor VSP 3000.

Variable temperature infrared spectra (VT IR) were recorded using the Perkin Elmer Spectrum 2000 spectrometer over the range of 400–4000 cm^{-1} with a medium slit width and a peak resolution of

2.0 cm^{-1}. The glass vessel with the precursor sample (≈ 100 mg) was placed in a home-made reactor tube as described earlier[49] and heated (from 30 to 380 °C) under dynamic vacuum (p = 1 Pa).

The surface morphology of the as-obtained layers was investigated by field-emission scanning electron microscopy using a ZEISS Supra60 SEM. Cross-sectional SEM investigations were carried out to determine the film thickness. Energy-dispersive X-ray analysis using a Bruker Quantax 400 system attached to a SEM was applied to determine the chemical composition of the films. The composition of the Ru samples was investigated by a PREVAC XPS system. Monochromatic aluminum K_α radiation (1486.6 eV) was provided by a VG Scienta MX 650 X-ray source and a monochromator. The energy distribution of the photoelectrons was measured with a VG Scienta EW3000 XPS/UPS/ARPES analyzer. This analyzer was operated at 200 eV pass energy with a step size of 200 meV and a measurement time of 1.5 s for each data point. Casa XPS 2.3.16 Pre-rel 1.4 software was used for the deconvolution of the XPS peaks. For the calculation of the atomic concentration, Scofield relative sensitivity factors (RSFs) were applied. These RSFs were corrected for a monochromator-analyzer angle of 52.55 °. For the escape depth correction in Casa XPS, a value of –0.7 was applied.

Diffraction data were collected with an Oxford Gemini S diffractometer using graphite-monochromated Mo-K_α radiation (**4a**–**f**) (λ = 0.71073 Å) at 120 K with oil-coated shock-cooled crystals. The structures were solved by direct methods and refined by full-matrix least-squares procedures on F^2.[50–52] All non-hydrogen atoms were refined anisotropically, and a riding model was employed in the refinement of the hydrogen atom positions. Graphics of the molecular structures were created by using SHELXTL and ORTEP.[53]

CCDC 1942921 (for **4a**), 1942922 (for **4b**), 1939984 (for **4c**), 1939985 (for **4d**), 1942920 (for **4e**), and 1939986 (for **4f**) contain the supplementary crystallographic data for this paper. These data can be obtained free of charge from The Cambridge Crystallographic Data Centre.

Precursor Synthesis and Characterization

General Synthesis Procedure for the Preparation of Ruthenium Complexes 4a–f: A tetrahydrofuran solution containing $Ru_3(CO)_{12}$ (**1**) (200 mg, 313 μmol), PEt_3 (**2**) (3.65 mL, 3.65 mmol; 1.0 M thf solution) and 4-methylpentan-2-one (18 mL) was refluxed for 30 min. Subsequently, the respective carboxylic acid (**3a**–**f**) (2.50 mmol) was added and the appropriate reaction solution was heated to reflux for 4 h. After cooling the reaction mixture to ambient temperature, all volatiles were removed in vacuo and the obtained residue was recrystallized from a hexane/diethyl ether mixture (*v*/*v*, 4 mL, ratio 10:1) at 10 °C.

Synthesis of $Ru(CO)_2(PEt_3)_2(O_2CCH_3)_2$ (4a): The title compound was synthesized according to the general synthetic procedure described above by using acetic acid (**3a**) (150 mg, 2.50 mmol). After recrystallization, **4a** was obtained as a colorless, crystalline solid. Yield: 375 mg (733 μmol, 78 % based on **1**). M.p. 125 °C; anal. calcd. for $C_{18}H_{36}O_6P_2Ru$: C 42.27; H 7.09; C 42.39; 7.19 H; IR data (KBr, $\tilde{\nu}/cm^{-1}$): 2976 m, 2940 m, 2920 m, 2885 m, 2038 vs, 1972 vs, 1941 m, 1614 s, 1461 m, 1426 m, 1385 s, 1369 s, 1320 s, 1255 m, 1035 s, 1007 m, 924 w, 770 s, 732 s, 669 m, 602 s, 553 w; ^{1}H NMR (500 MHz, $CDCl_3$, δ): 1.09–1.20 (m, 18 H, PCH_2CH_3), 1.84–1.93 (m, 12 H, PCH_2CH_3), 2.02 (s, 6 H, CH_3); $^{13}C\{^1H\}$ NMR (125 MHz, $CDCl_3$, δ): 7.3 (s, PCH_2CH_3), 16.2 (t, J_{CP} = 13.4 Hz, PCH_2CH_3), 23.75 (s, CH_3), 177.27 (s, O_2C), 197.8 (t, J_{CP} = 11.6 Hz, CO); $^{31}P\{^1H\}$ NMR (202 MHz, $CDCl_3$, δ): 23.10; HRMS (ESI-TOF, *m*/*z*): calcd. for $C_{16}H_{33}O_4P_2Ru$: 453.0915, found 453.0897 $[M - O_2CCH_3]^+$.

Crystal Data for 4a: $C_{18}H_{36}O_6P_2Ru$, M_r = 511.48 g/mol, monoclinic, $P2_1/n$, λ = 0.71073 Å, a = 8.6296(2) Å, b = 11.7136(2) Å, c = 24.0473(5) Å, β = 99.237(2)°, V = 2399.27(9) Å^3, Z = 4, ρ_{calcd} = 1.416 mg cm^{-3}, μ = 0.814 mm^{-1}, T = 120 K, Θ range 2.957–24.993°, 20135 reflections collected, 4208 independent reflections (R_{int} = 0.0279), R_1 = 0.0223, wR_2 = 0.0490 [$I > 2\sigma(I)$].

Synthesis of $Ru(CO)_2(PEt_3)_2(O_2CCH_2CH_3)_2$ (4b): The title complex was synthesized according to the general synthetic procedure described earlier by using propionic acid (**3b**) (185 mg, 2.50 mmol). After recrystallization, **4b** was obtained as a colorless, crystalline solid. Yield: 279 mg (517 μmol, 55 % based on **1**). M.p. 134 °C; anal. calcd. for $C_{20}H_{40}O_6P_2Ru$: C 44.52; H 7.47; C 44.07; H 7.41; IR data (KBr, $\tilde{\nu}/cm^{-1}$): 2973 m, 2940 m, 2883 m; 2036 vs, 1971 vs, 1611 s, 1458 m, 1420 m, 1347 m, 1275 m, 1074 w, 1034 m, 880 w, 730 m, 604 w; ^{1}H NMR (500 MHz, $CDCl_3$, δ): 1.08–1.16 (m, 24 H, $O_2CH_2CH_3$, PCH_2CH_3), 1.79–1.90 (m, 12 H, PCH_2CH_3), 2.27 (q, J_{HH} = 7.6 Hz, 4 H, $O_2CH_2CH_3$); $^{13}C\{^1H\}$ NMR (125 MHz, $CDCl_3$, δ): 7.3 (s, PCH_2CH_3), 11.0 (s, $O_2CH_2CH_3$) 16.1 (t, J_{CP} = 13.4 Hz, PCH_2CH_3), 30.3 (s, $O_2CH_2CH_3$), 180.1 (s, O_2C), 197.9 (t, J_{CP} = 11.7 Hz, CO); $^{31}P\{^1H\}$ NMR (202 MHz, $CDCl_3$, δ): 22.94; HRMS (ESI-TOF, *m*/*z*): calcd. for $C_{17}H_{35}O_4P_2Ru$: 467.1061, found 467.1053 $[M - O_2CCH_2CH_3]^+$.

Crystal Data for 4b: $C_{20}H_{40}O_6P_2Ru$, M_r = 539.53 g/mol, triclinic, $P\bar{1}$, λ = 0.71073 Å, a = 9.4534(4) Å, b = 11.7382(6) Å, c = 13.0643(7) Å, α = 75.691(4)°, β = 72.158(4)°, γ = 68.117(5)°, V = 1265.95(12) Å^3, Z = 2, ρ_{calcd} = 1.415 mg cm^{-3}, μ = 0.776 mm^{-1}, T = 120 K, Θ range 3.217–24.999°, 13294 reflections collected, 4400 independent reflections (R_{int} = 0.0272), R_1 = 0.0228, wR_2 = 0.0503 [$I > 2\sigma(I)$].

Synthesis of $Ru(CO)_2(PEt_3)_2[O_2CCH(CH_3)_2]_2$ (4c): Complex **4c** was synthesized according to the general synthetic procedure described earlier by using isobutyric acid (**3c**) (220 mg, 2.50 mmol). After recrystallization, **4c** was obtained as a colorless, crystalline solid. Yield: 485 mg (855 μmol, 91 % based on **1**). M.p. 142 °C; anal. calcd. for $C_{22}H_{44}O_6P_2Ru$: C 46.55; H 7.81; C 46.54; H 7.91; IR data (KBr, $\tilde{\nu}/cm^{-1}$): 2970 m, 2940 m, 2883 m; 2037 vs, 1970 vs, 1612 s, 1458 m, 1419 m, 1344 m, 1265 m, 1085 w, 1034 m, 840 w, 730 m, 603 w; ^{1}H NMR (500 MHz, $CDCl_3$, δ): 1.08–1.18 (m, 30 H, $O_2CCH(CH_3)_2$, PCH_2CH_3), 1.82–1.89 (m, 12 H, PCH_2CH_3), 2.48 (dt, J_{HH} = 14.0, 7.0 Hz, 2 H, $O_2CCH(CH_3)_2$); $^{13}C\{^1H\}$ NMR (125 MHz, $CDCl_3$, δ): 7.4 (s, PCH_2CH_3), 15.9 (t, J_{CP} = 13.4 Hz, PCH_2CH_3), 20.5 (s, $O_2CCH(CH_3)_2$), 36.1 (s, $O_2CCH(CH_3)_2$), 182.5 (s, O_2C), 197.9 (t, J_{CP} = 11.7 Hz, CO); $^{31}P\{^1H\}$ NMR (202 MHz, $CDCl_3$, δ): 22.23; HRMS (ESI-TOF, *m*/*z*): calcd. for $C_{18}H_{37}O_4P_2Ru$: 481.1199, found 481.1210 $[M - O_2CCH(CH_3)_2]^+$.

Crystal Data for 4c: $C_{22}H_{44}O_6P_2Ru$, M_r = 567.58 g/mol, monoclinic, $P2_1/c$, λ = 0.71073 Å, a = 9.2375(2) Å, b = 11.8393(4) Å, c = 24.9200(8) Å, β = 99.418(3)°, V = 2688.65(14) Å^3, Z = 4, ρ_{calcd} = 1.402 mg cm^{-3}, μ = 0.734 mm^{-1}, T = 120 K, Θ range 3.510–25.498°, 14223 reflections collected, 4968 independent reflections (R_{int} = 0.0188), R_1 = 0.0224, wR_2 = 0.0500 [$I > 2\sigma(I)$].

Synthesis of $Ru(CO)_2(PEt_3)_2[O_2CC(CH_3)_3]_2$ (4d): Complex **4d** was synthesized according to the general synthetic procedure described earlier by using pivalic acid (**3d**) (256 mg, 2.50 mmol). After recrystallization, **4d** was obtained as a colorless, crystalline solid. Yield: 386 mg (648 μmol, 69 % based on **1**). M.p. 135 °C; anal. calcd. for $C_{24}H_{48}O_6P_2Ru$: C 48.39; H 8.12; C 48.33; H 8.10; IR data (KBr, $\tilde{\nu}/cm^{-1}$): 2970 m, 2940 m, 2883 m; 2039 vs, 1973 vs, 1944 w, 1602 s, 1570 w, 1478 w, 1462 w, 1420 w, 1392 m, 1332 s, 1214 m, 1037 m, 887 w, 775 m, 603 w, 505 w; ^{1}H NMR (500 MHz, $CDCl_3$, δ): 1.08–1.18 (m, 36 H, $O_2CC(CH_3)_3$, PCH_2CH_3), 1.81–1.91 (m, 12 H, PCH_2CH_3); $^{13}C\{^1H\}$ NMR (125 MHz, $CDCl_3$, δ): 7.4 (s, PCH_2CH_3), 15.7 (t, J_{CP} = 13.4 Hz, PCH_2CH_3), 28.7 (s, $O_2CC(CH_3)_3$), 39.4 (s, $O_2CC(CH_3)_2$), 183.6 (s, O_2C), 197.9 (t, J_{CP} = 10.1 Hz, CO); $^{31}P\{^1H\}$ NMR (202 MHz, $CDCl_3$,

δ): 21.55; HRMS (ESI-TOF, *m/z*): calcd. for $C_{18}H_{37}O_4P_2Ru$: 495.1343, found 495.1367 [M – $O_2CC(CH_3)_3$]$^+$.

Crystal Data for 4d: $C_{24}H_{48}O_6P_2Ru$, M_r = 595.63 g/mol, monoclinic, $P\bar{1}$, λ = 0.71073 Å, a = 9.6756(10) Å, b = 12.0718(7) Å, c = 12.7782(10) Å, α = 87.996(6)°, β = 83.246(8)°, γ = 87.256(7)°, V = 1479.8(2) Å^3, Z = 2, ρ_{calcd} = 1.337 mg cm^{-3}, μ = 0.670 mm^{-1}, T = 120 K, Θ range 3.300–24.999°, 9333 reflections collected, 5156 independent reflections (R_{int} = 0.0353), R_1 = 0.0872, wR_2 = 0.2102 [$I > 2\sigma(I)$].

Synthesis of $Ru(CO)_2(PEt_3)_2(O_2CCH_2OCH_3)_2$ (4e): Complex **4e** was synthesized according to the general synthetic procedure described earlier by using 2-methoxyacetic acid (**3e**) (225 mg, 2.50 mmol). After appropriate work-up, **4e** was obtained as a colorless, crystalline solid. Yield: 514 mg (900 μmol, 90 % based on **1**). M.p. 112 °C; anal. calcd. for $C_{20}H_{40}O_8P_2Ru$: C 42.03; H 7.05; C 41.96; H 7.12; IR data (KBr, $\tilde{\nu}$/cm^{-1}): 2965 m, 2935 m, 2884 m; 2819 m, 2038 vs, 1971 vs, 1639 s, 1450 m, 1418 m, 1376 m, 1273 m, 1038 w, 1016 m, 909 w, 730 m, 606 w; ^{1}H NMR (500 MHz, $CDCl_3$, δ): 1.08–1.18 (m, 18 H, PCH_2CH_3), 1.85–1.94 (m, 12 H, PCH_2CH_3), 3.42 (s, 6 H, $O_2CCH_2OCH_3$), 3.93 (s, 4 H, $O_2CCH_2OCH_3$); ^{13}C{^{1}H} NMR (125 MHz, $CDCl_3$, δ): 7.3 (s, PCH_2CH_3), 16.2 (t, J_{CP} = 13.5 Hz, PCH_2CH_3), 59.0 (s, $O_2CCH_2OCH_3$), 72.2 (s, $O_2CCH_2CH_3$), 175.6 (s, O_2C), 197.3 (t, J_{CP} = 11.7 Hz, *C*O); ^{31}P{^{1}H} NMR (202 MHz, $CDCl_3$, δ): 23.01; HRMS (ESI-TOF, *m/z*): calcd. for $C_{20}H_{40}O_8P_2Ru$: 595.1132, found 595.1140 [M + Na]$^+$.

Crystal Data for 4e: $C_{20}H_{40}O_8P_2Ru$, M_r = 571.53 g/mol, orthorhombic, $Pca2_1$, λ = 0.71073 Å, a = 25.3255(10) Å, b = 8.6939(3) Å, c = 11.9751(4) Å, V = 2636.65(16) Å^3, Z = 4, ρ_{calcd} = 1.440 mg cm^{-3}, μ = 0.755 mm^{-1}, T = 120 K, Θ range 3.218–24.999°, 6487 reflections collected, 3976 independent reflections (R_{int} = 0.0294), R_1 = 0.0307, wR_2 = 0.0606 [$I > 2\sigma(I)$].

Synthesis of $Ru(CO)_2(PEt_3)_2(O_2CCF_3)_2$ (4f): Complex **4f** was synthesized according to the general synthetic procedure described earlier by using trifluoroacetic acid (**3f**) (285 mg, 2.50 mmol). After appropriate work-up, **4f** was obtained as a colorless, crystalline solid. Yield: 566 mg (914 μmol, 97 % based on **1**). M.p. 165 °C; anal. calcd. for $C_{18}H_{30}O_6F_6P_2Ru$: C 34.79; H 5.19; C 35.14; H 5.09; IR data (KBr, $\tilde{\nu}$/cm^{-1}): 2982 m, 2947 m, 2891 m, 2056 vs, 1994 vs, 1685 s, 1465 m, 1414 m, 1388 w, 1195 s, 1143 s, 1034 w, 850 m, 793 m, 768 m, 731 m, 669 m, 599 m; ^{1}H NMR (500 MHz, $CDCl_3$, δ): 1.08–1.19 (m, 18 H, PCH_2CH_3), 1.82–1.93 (m, 12 H, PCH_2CH_3); ^{13}C{^{1}H} NMR (125 MHz, $CDCl_3$, δ): 7.0 (s, PCH_2CH_3), 16.0 (t, J_{CP} = 13.9 Hz, PCH_2CH_3), 115.5 (q, J_{CF} = 289.9 Hz, CF_3), 167.7 (q, J_{CF} = 36.9 Hz O_2C), 196.2 (t, J_{CP} = 11.3 Hz, *C*O); ^{31}P{^{1}H} NMR (202 MHz, $CDCl_3$, δ): 22.64; HRMS (ESI-TOF, *m/z*): calcd. for $C_{16}H_{30}O_4F_3P_2Ru$: 507.0614, found 507.0589 [M – O_2CCF_3]$^+$.

Crystal Data for 4f: $C_{18}H_{30}O_6F_6P_2Ru$, M_r = 619.43 g/mol, monoclinic, $P2_1/c$, λ = 0.71073 Å, a = 8.7216(5) Å, b = 11.7899(7) Å, c = 24.8182(16) Å, β = 100.005(6)°, V = 2513.2(3) Å^3, Z = 4, ρ_{calcd} = 1.637 mg cm^{-3}, μ = 0.826 mm^{-1}, T = 115 K, Θ range 2.934–24.994°, 13249 reflections collected, 4382 independent reflections (R_{int} = 0.0520), R_1 = 0.0424, wR_2 = 0.0794 [$I > 2\sigma(I)$].

Theoretical Approach

The study used Becke's three-parameter hybrid functional applying non-local correlation provided by Lee, Yang, and Parr (B3LYP).[54] Here, the 3-21G and 6-311G* basis sets for Ru and the other atoms were applied, too, as it is implemented in the Gaussian package.[55–58] These sets were used to precisely describe the system under study and to facilitate computations. The comparison of the bond lengths and angles for complexes **4a**–**f** prove correctness of the basis sets chosen. The deviation of less than 2 % in average was evaluated for bond lengths and that for angles was less than 1 %. The structures of the complexes and their fragments were optimized without any symmetry constraints. The fragment anions, cations and fragments with a zero charge were evaluated to interpret the experimental results. We assume that an electron was not released during decomposition of the parent complexes, i.e. the total charge of the fragments formed was equal to 0. It allowed us to reduce the number of the possible ways of the above layer formation, although it remained high enough (the total number ways investigated is equal ≈ 140). The fragment appearance energies were calculated as the difference between the total energy of the investigated compounds and the sum of the energies of their fragments predicted to find and analyze the most probable ways of the above layer formation. The smallest energy of appearance indicated the energetically more probable way of fragment formation. The vibrational analysis of **4a**–**f** of interest was used to estimate the zero-point corrections. These corrections were included in the calculations of the total energy of the complexes.

Acknowledgments

This project has received funding from the European Social Fund (ESF; A. P.). We acknowledge Cornelia Kowol and Dirk Rittrich for performing the SEM/EDX measurements and Natalia Rüffer for performing TG as well as the vapor pressure studies. Furthermore, we gratefully acknowledge Janine Freytag and Ute Stöß for performing elemental analysis measurements. The authors are grateful for the high-performance computing resources provided by the Information Technology Open Access Centre of Vilnius University.

Keywords: Ruthenium · Solid-state structures · Thermogravimetry · Density functional calculations · Chemical vapor deposition

[1] A. E. Kaloyeros, E. T. Eisenbraun, K. Dunn, O. van der Straten, *Chem. Eng. Commun.* **2011**, *198*, 1453–1481.
[2] A. Tuchscherer, C. Georgi, N. Roth, D. Schaarschmidt, T. Rüffer, T. Waechtler, S. E. Schulz, S. Oswald, T. Gessner, H. Lang, *Eur. J. Inorg. Chem.* **2012**, *2012*, 4867–4876.
[3] M. L. Green, M. E. Gross, L. E. Papa, K. J. Schnoes, D. Brasen, *J. Electrochem. Soc.* **1985**, *132*, 2677–2685.
[4] S. Y. Kang, C. S. Hwang, H. J. Kim, *J. Electrochem. Soc.* **2005**, *152*, C15–C19.
[5] T. N. Arunagiri, Y. Zhang, O. Chyan, M. El-Bouanani, M. J. Kim, K. H. Chen, C. T. Wu, L. C. Chen, *Appl. Phys. Lett.* **2005**, *86*, 083104.
[6] D. C. Perng, J. Bin Yeh, K. C. Hsu, *Appl. Surf. Sci.* **2008**, *254*, 6059–6062.
[7] D. Josell, D. Wheeler, C. Witt, T. P. Moffat, *Electrochem. Solid-State Lett.* **2003**, *6*, C143–C145.
[8] J. Shin, A. Waheed, K. Agapiou, W. A. Winkenwerder, H. W. Kim, R. A. Jones, G. S. Hwang, J. G. Ekerdt, *J. Am. Chem. Soc.* **2006**, *128*, 16510–16511.
[9] O.-K. Kwon, J.-H. Kim, H.-S. Park, S.-W. Kang, *J. Electrochem. Soc.* **2004**, *151*, G109–G112.
[10] O.-K. Kwon, S.-H. Kwon, H.-S. Park, S.-W. Kang, *J. Electrochem. Soc.* **2004**, *151*, C753–C756.
[11] S.-H. Choi, T. Cheon, S.-H. Kim, D.-H. Kang, G.-S. Park, S. Kim, *J. Electrochem. Soc.* **2011**, *158*, D351–D356.
[12] J. J. Tan, X. P. Qu, Q. Xie, Y. Zhou, G. P. Ru, *Thin Solid Films* **2006**, *504*, 231–234.
[13] T. P. Moffat, M. Walker, P. J. Chen, J. E. Bonevich, W. F. Egelhoff, L. Richter, C. Witt, T. Aaltonen, M. Ritala, M. Leskelä, D. Josell, *J. Electrochem. Soc.* **2006**, *153*, C37–C50.
[14] T. Cheon, S.-H. Choi, S.-H. Kim, D.-H. Kang, *Electrochem. Solid-State Lett.* **2011**, *14*, D57–D61.
[15] J. Jeschke, S. Möckel, M. Korb, T. Rüffer, K. Assim, M. Melzer, G. Herwig, C. Georgi, S. E. Schulz, H. Lang, *J. Mater. Chem. C* **2016**, *4*, 2319–2328.

[16] D. C. Perng, K. C. Hsu, S. W. Tsai, J. Bin Yeh, *Microelectron. Eng.* **2010**, *87*, 365–369.
[17] J. Shin, H. W. Kim, G. S. Hwang, J. G. Ekerdt, *Surf. Coat. Technol.* **2007**, *201*, 9256–9259.
[18] J. Shin, A. Waheed, W. A. Winkenwerder, H. W. Kim, K. Agapiou, R. A. Jones, G. S. Hwang, J. G. Ekerdt, *Thin Solid Films* **2007**, *515*, 5298–5307.
[19] D. E. Bost, J. G. Ekerdt, *Thin Solid Films* **2014**, *558*, 160–164.
[20] D. E. Bost, H. W. Kim, C. Y. Chou, G. S. Hwang, J. G. Ekerdt, *Thin Solid Films* **2017**, *622*, 56–64.
[21] H. Lang, S. Dietrich in Comprehensive Inorganic Chemistry II (Eds.: J. Reedijk, K. Poeppelmeier), *Metals - Gas-Phase Deposition and Applications*, Elsevier Ltd., Amsterdam, **2013**, vol. 2, pp. 211–269.
[22] L. B. Henderson, J. G. Ekerdt, *Thin Solid Films* **2009**, *517*, 1645–1649.
[23] J. Shin, H.-W. Kim, K. Agapiou, R. A. Jones, G. S. Hwang, J. G. Ekerdt, *J. Vac. Sci. Technol. A* **2008**, *26*, 974–979.
[24] T. T. Kodas, M. J. Hampden-Smith, *The Chemistry of Metal CVD*, WILEY-VCH, Weinheim, **1994**.
[25] J. Jeschke, C. Georgi, H. Lang, Ruthenium-Precursoren Zur Abscheidung von Rutheniumschichten, Herstellung Und Verwendung, DE 10 **2014** 205 342 A1 (**2015**).
[26] M. Bianchi, P. Frediani, U. Matteoli, G. Menchi, F. Piacenti, G. Petrucci, *J. Organomet. Chem.* **1983**, *259*, 207–214.
[27] J. Jeschke, C. Gäbler, M. Korb, T. Rüffer, H. Lang, *Eur. J. Inorg. Chem.* **2015**, 2939–2947.
[28] J. Jeschke, M. Korb, T. Rüffer, C. Gäbler, H. Lang, *Adv. Synth. Catal.* **2015**, *357*, 4069–4081.
[29] J. H. Nelson, *Concepts Magn. Reson.* **2002**, *14*, 19–78.
[30] R. K. Harris, *Can. J. Chem.* **1964**, *42*, 2275–2281.
[31] H. G. Metzinger, *Org. Magn. Reson.* **1971**, *3*, 485–494.
[32] B. F. G. Johnson, R. D. Johnston, J. Lewis, I. G. Williams, *J. Chem. Soc. A* **1971**, 689–691.
[33] G. B. Deacon, R. J. Phillips, *Coord. Chem. Rev.* **1980**, *33*, 227–250.
[34] F. J. Lee, Y. Chi, C. S. Liu, P. F. Hsu, T. Y. Chou, S. M. Peng, G. H. Lee, *Chem. Vap. Deposition* **2001**, *7*, 99–101.
[35] G. Miessler, P. Fischer, D. Tarr, *Inorganic Chemistry*, Pearson Education, Upper Saddle River, N. J. **2014**.
[36] Y. H. Lai, C. T. Yeh, H. J. Lin, C. Te Chen, W. H. Hung, *J. Phys. Chem. B* **2002**, *106*, 1722–1727.
[37] K.-M. Chang, I.-C. Deng, H.-Y. Lin, *J. Electrochem. Soc.* **1999**, *146*, 3092–3096.
[38] *NIST X-ray Photoelectron Spectroscopy Database, Version 4.1*, National Institut Of Standards Technology, Gaithersburg, USA, **2012**.
[39] D. Briggs, M. P. Seah, *Practical Surface Analysis by Auger and X-ray Photoelectron Spectroscopy*, Wiley & Sons, Chichester, UK, **1992**.
[40] H. Y. H. Chan, C. G. Takoudis, M. J. Weaver, *J. Catal.* **1997**, *172*, 336–345.
[41] J. Y. Shen, A. Adnot, S. Kaliaguine, *Appl. Surf. Sci.* **1991**, *51*, 47–60.
[42] D. E. Starr, H. Bluhm, *Surf. Sci.* **2013**, *608*, 241–248.
[43] E. Shincho, C. Egawa, S. Naito, K. Tamaru, *Surf. Sci.* **1985**, *149*, 1–16.
[44] A. Ghicov, H. Tsuchiya, J. M. MacAk, P. Schmuki, *Electrochem. Commun.* **2005**, *7*, 505–509.
[45] C. A. Strydom, H. J. Strydom, *Inorg. Chim. Acta* **1989**, *159*, 191–195.
[46] I. Jipa, M. A. Siddiqi, R. A. Siddiqui, B. Atakan, H. Marbach, T. Cremer, F. Maier, H. P. Steinrück, K. Danova, N. Popovska, F. W. Heinemann, U. Zenneck, *Chem. Vap. Deposition* **2011**, *17*, 15–21.
[47] A. Schneider, N. Popovska, F. Holzmann, H. Gerhard, C. Topf, U. Zenneck, *Chem. Vap. Deposition* **2005**, *11*, 99–105.
[48] K. Jacobi, *Phys. Status Solidi A* **2000**, *177*, 37–51.
[49] P. Piszczek, A. Grodzicki, M. Richert, A. Radtke, *Mater. Sci. - Poland* **2005**, *23*, 663–670.
[50] G. M. Sheldrick, *Acta Crystallogr., Sect. A* **1990**, *46*, 467–473.
[51] G. M. Sheldrick, *SHELXL-97, Program for Crystal Structure Refinement*, Universität Göttingen, **1997**.
[52] G. M. Sheldrick, *Acta Crystallogr., Sect. A* **2008**, *64*, 112–122.
[53] L. J. Farrugia, *J. Appl. Crystallogr.* **2012**, *45*, 849–854.
[54] A. D. Becke, *J. Chem. Phys.* **1993**, *98*, 5648–5652.
[55] K. D. Dobbs, W. J. Hehre, *J. Comput. Chem.* **1987**, *8*, 880–893.
[56] R. Krishnan, J. S. Binkley, R. Seeger, J. A. Pople, *J. Chem. Phys.* **1980**, *72*, 650–654.
[57] M. J. Frisch, J. A. Pople, J. S. Binkley, *J. Chem. Phys.* **1984**, *80*, 3265–3269.
[58] M. J. Frisch, G. W. Trucks, H. B. Schlegel, G. E. Scuseria, M. A. Robb, J. R. Cheeseman, J. A. Montgomery Jr., T. Vreven, K. N. Kudin, J. C. Burant, J. M. Millam, S. S. Iyengar, J. Tomasi, V. Barone, B. Mennucci, M. Cossi, G. Scalmani, N. Rega, G. A. Petersson, H. Nakatsuji, M. Hada, M. Ehara, K. Toyota, R. Fukuda, J. Hasegawa, M. Ishida, T. Nakajima, Y. Honda, O. Kitao, H. Nakai, M. Klene, X. Li, J. E. Knox, H. P. Hratchian, J. B. Cross, V. Bakken, C. Adamo, J. Jaramillo, R. Gomperts, R. E. Stratmann, O. Yazyev, A. J. Austin R. Cammi, C. Pomelli, J. W. Ochterski, P. Y. Ayala, K. Morokuma, G. A. Voth, P. Salvador, J. J. Dannenberg, V. G. Zakrzewski, S. Dapprich, A. D. Daniels, M. C. Strain, O. Farkas, D. K. Malick, A. D. Rabuck, K. Raghavachari, J. B. Foresman, J. V. Ortiz, Q. Cui, A. G. Baboul, S. Clifford, J. Cioslowski, B. B. Stefanov, G. Liu, A. Liashenko, P. Piskorz, I. Komaromi, R. L. Martin, D. J. Fox, T. Keith, M. A. Al-Laham, C. Y. Peng, A. Nanayakkara, M. Challacombe, P. M. W. Gill, B. Johnson, W. Chen, M. W. Wong, C. Gonzalez, J. A. Pople, *Gaussian 03*, **2004**.

Received: December 10, 2019